Silicon and polymer nanophotonic devices based on photonic crystals

Wei Jiang[a,b*], Yongqiang Jiang[a], Lanlan Gu[a], Li Wang[a], Xiaonan Chen[a], & Ray T. Chen[a]
[a]Microelectronics Research Center, University of Texas, Austin, TX 78758
[b]Omega Optics, Inc., Austin, TX, 78758

ABSTRACT

Photonic crystals (PhCs) provide a promising nanophotonic platform for developing novel optoelectronic devices with significantly reduced device size and power consumption. Silicon nanophotonics is anticipated to play a pivotal role in the future nano-system integration owing to the maturity of sub-micron silicon complementary metal oxide semiconductor (CMOS) technology. An ultra-compact silicon modulator was experimentally demonstrated based on silicon photonic crystal waveguides. Modulation operation was achieved by carrier injection into an 80-micron-long silicon PhC waveguide of a Mach-Zehnder interferometer (MZI) structure. The driving current to obtain a phase shift of π across the active region was as low as 0.15 mA, owing to slow light group velocity in PhC waveguides. The modulation depth was 92%. The electrode between the two waveguide arms of the MZI structure was routed to the space outside the MZI. In real devices, this planarized routing design would be essential to integrating the silicon modulator with electrical driving circuitry on a single silicon chip. For laboratory test, this routing scheme also eliminated the need of placing a bulky pad between the two arms and gave our modulator a distinctive slim profile and a much smaller footprint. Polymeric photonic crystals were designed for superprism based laser beam steering applications, and were fabricated by nano-imprint and other techniques.

Keywords: photonic crystal, silicon photonics, slow light, polymer nanophotonics, nano-imprint

1. INTRODUCTION

The beginning of 21st century witnesses the pervasive presence of nanostructures and nanofabrication in science and technology. In photonics, nanoscale structures, particularly photonic crystals,[1-2] hold the promise of achieving the same function in a significantly reduced device size with reduced power consumption (e.g. thresholdless lasers based on photonic crystal cavities[1]). Photonic crystals are a new class of artificial materials that provide novel capabilities for the control and manipulation of light. These materials can be viewed ideally as a composite of a periodic array of low- or high-dielectric scatterers in a homogeneous high- or low-dielectric matrix, respectively. A real example is a single slab of semiconductor (high-dielectric) containing a periodic array of air-holes (low-dielectric), which forms a two-dimensional (2D) photonic crystal. The underlying concept of photonic crystals stems from early work by Yablonovitch[1] and John.[2] The periodic dielectric structure of a photonic crystal causes photons to form photonic bands and photonic bandgaps (PBG) in the same fashion that electrons form energy bands and bandgaps in an atomic crystal. If the frequency of light (or photon) falls inside a PBG, the photonic crystal will reflect light totally regardless of its incident angle, which provides a unique opportunity for strong light confinement. Optical waveguides based on photonic crystal line defects (shown in Fig. 1(a)),[3-6] the so-called photonic crystal waveguides (PCWs), have been demonstrated to slow down light significantly.[3] Such an extraordinary dispersion capability has a profound impact on the phase change over a segment of photonic crystal waveguides. For example, when incorporated in silicon Mach-Zehnder modulators, photonic crystal waveguides lead to significant enhancement of the modulation efficiency, which in turn allows us to reduce the modulator electrode length by several orders of magnitude.[7,8]

2. SILICON NANOPHOTONIC MODULATORS AND OTHER DEVICES

2.1 Silicon photonics

In the context of microelectronics, silicon has been the optimal material for microelectronics for decades, but it has only relatively recently been considered as a viable option for photonics.[9-11] From the material perspective, silicon has an indirect bandgap and no χ^2-nonlinearity. These intrinsic properties stymied the efforts of making silicon lasers and

* jiang@ece.utexas.edu, phone: 512-826-4621, 512-996-8833 x601

Optoelectronic Integrated Circuits VIII, edited by Louay A. Eldada, El-Hang Lee,
Proc. of SPIE Vol. 6124, 612410, (2006) · 0277-786X/06/$15 · doi: 10.1117/12.674116

silicon modulators for a very long time. On the other hand, silicon is transparent in the range of optical telecommunication wavelengths, 1.3 μm and 1.55 μm, and has a high refractive index that allows for the fabrication of high-index-contrast nano-photonic structures. These allow low-loss optical waveguides and dense planar lightwave circuits to be manufactured on silicon. As silicon photonics technology can be made compatible with conventional complementary metal-oxide-semiconductor (CMOS) processing, monolithic integration of silicon photonic devices with advanced electronics on single silicon substrate becomes possible if integrated light sources and modulators can be made on silicon. With these two key elements added to the arsenal of silicon photonics, numerous photonic micro- or nano-systems can be built on silicon by integrating a large number of such optoelectronic elements, and enormous potential in optical interconnects, telecommunications, consumer electronics, and entertainment would unfold.

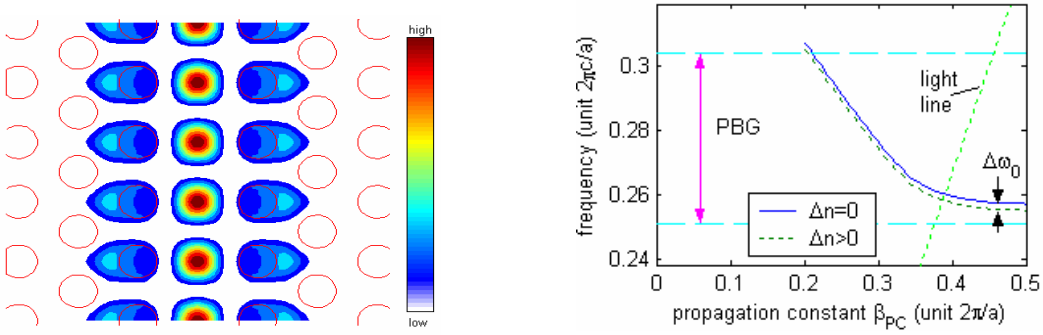

(a) (b)

Figure 1 Photonic crystal waveguide (a) electric field profile of a guided mode of a photonic crystal waveguide, where the central row of air holes is removed to form a linear defect. (b) Photonic crystal waveguide dispersion relation, used to illustrate the principle of enhancing modulation efficiency through highly dispersive photonic crystal waveguide.

The incorporation of silicon photonic elements could generate huge benefits unavailable in prior purely electronic technologies. For example, future computers that could be hundreds times faster need to relay overwhelming large-volume data on a silicon chip. The current electrical interconnect technology based on copper wires is almost certain to fail at such high data rates. Optical interconnects is widely regarded as a promising technology for tomorrow's on-chip interconnection.[12] With the ultimate success of silicon photonics, optical interconnects could potentially forgo III-V material based devices and overcome all of the difficulties associated with the hybrid integration and packaging. Although promising progress has been made in recent years in silicon lasers,[13-14] the pursuit of the electrically pumped silicon laser is still underway. In this paper, we will limit the scope of our discussions to silicon modulators. More specifically, we will focus our discussions to silicon modulators based on photonic crystal waveguides. However, we believe that the CMOS compatible processing technology we successfully developed for our modulator could lay the foundation for further development of photonic crystal based silicon light emitting devices.

2.2 Principle of enhancing modulation efficiency through photonic crystal waveguides

Silicon optical modulators have been studied for almost two decades.[15-23] Kerr effect, Franz-Keldysh effect, and plasma dispersion effect are the main mechanisms for modulating the refractive index of silicon. It has been long established that the former two effects have very low modulation efficiency, leaving plasma dispersion effect the prime choice.[9] For the plasma dispersion effect, charge carriers are injected into silicon or induced in silicon through biased electrodes; and the refractive index changes with the increased carrier concentration in silicon. Experiments have established that at the output end of a silicon waveguide, the phase change $\Delta\phi$ due to carrier concentration variation is almost a linear function of the waveguide length L and the applied voltage V on the electrodes[15]

$$\Delta\phi = \Delta n \cdot k_0 L = \alpha V L \,, \qquad (1)$$

where k_0 is the wavevector in vacuum, and one immediately deduces that the refractive index variation of silicon is a linear function of V. The phase change per applied voltage per electrode length is

$$\frac{\Delta\phi}{VL}=\alpha=\frac{\Delta n\cdot k_0}{V} \quad . \qquad (2)$$

For optical intensity modulators, the Mach-Zehnder structure that converts a phase modulation into an intensity modulation is most widely used. Consider a typical dispersion relation for a PCW mode shown in Fig. 1(b). If the refractive index of the waveguide core material (*i.e.* silicon) varies by an amount of Δn, the dispersion curve will shift vertically by an amount $\Delta\omega_0$. For a fixed frequency of light, the propagation constant β_{PC} of PCW changes as $\Delta\beta_{PC}=\frac{d\beta_{PC}}{d\omega}\Delta\omega_0$, which grows significantly whenever the group velocity $\frac{d\omega}{d\beta_{PC}}$ approaches zero, e.g. on the right-most segment of dispersion curve in Fig. 1(b). Such an extraordinary growth of $\Delta\beta_{PC}$ directly leads to a significant enhancement of phase modulation efficiency because the phase change is related to the change of propagation constant and waveguide length L as $\Delta\phi_{PC}=\Delta\beta_{PC}\times L$. The phase change per applied voltage per electrode length for a PCW is given by

$$\frac{\Delta\phi_{PC}}{VL}=\frac{\Delta\beta_{PC}L}{VL}=\frac{d\beta_{PC}}{d\omega}\frac{\Delta\omega_0}{V}. \qquad (3)$$

Evidently, whenever the group velocity $\frac{d\omega}{d\beta_{PC}}$ approaches zero, the modulation efficiency $\frac{\Delta\phi_{PC}}{VL}$ will grow significantly. The efficiency that a photonic crystal waveguide boosts up the phase change per voltage per electrode length when compared with a conventional Mach-Zehnder modulator is given by

$$A=\frac{\Delta\phi_{PC}/VL}{\Delta\phi/VL}=\frac{d\beta_{PC}}{d\omega}\frac{\Delta\omega_0}{\Delta n\cdot k_0}, \qquad (4)$$

where the $\frac{\Delta\phi}{VL}$ for a conventional waveguide is given in Eq. (2.2). In principle, the factor A could rise indefinitely at the bandedge of the guided mode. In practice, the observable or useful range of A is determined by bandwidth, optical loss and many other factors.

2.3 Modulator design and fabrication

We have conceived several structural configurations of a Mach-Zehnder silicon modulator based on photonic crystal waveguides. We have conducted preliminary optical and electrical simulations for each structure and also have analyzed the processing steps for fabricating each structure. Particularly, the finite element method was employed to evaluate the electrical resistance of a perforated silicon-on-insulator slab. We concluded that the presence of air holes shall not change the resistance of the slab by more than one order of magnitude for typical photonic crystal waveguide parameters. This allows us to quickly estimate the resistance value of the photonic crystal region in evaluating current and heating issue of the devices.

In choosing the structure shown in Fig. 2, we considered the electrical routing, ease of fabrication, and many other factors. The planarized structure we chose greatly simplified the fabrication process and improved the device yield. Furthermore, it allowed the electrode located between the two arms of the Mach-Zehnder structure to be routed to assumed peripheral driver circuits through an in-plane metal wire. This critical feature makes our device *immediately ready to be integrated with electronics on a single silicon chip*.

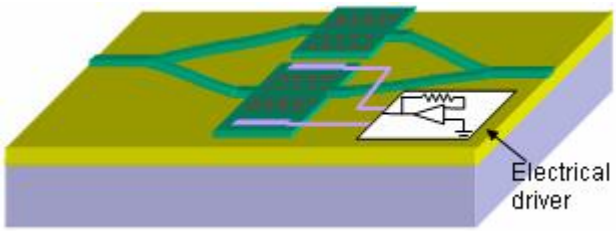

Figure 2 A planarized Mach-Zehnder modulator based on silicon photonic crystal waveguides. The waveguiding structures are formed on a silicon-on-insulator wafer (oxide: yellow; top silicon: green). The electrode (light purple) between the two arms are routed to outside the space between two arms, connecting to the driving circuitry that could be integrated on the same silicon chip.

To fabricate the ultra-compact silicon MZI modulator, the designed PhC waveguides, rib waveguides, and Y-junctions were first fabricated on a SOI wafer. Boron ions were implanted at 25 keV with a peak concentration of 2×10^{17} cm^{-3} into an N-type Si substrate with the doping concentration of 1×10^{14} cm^{-3}. Internally, we called the structure in Fig. 2 a *PIP* structure.

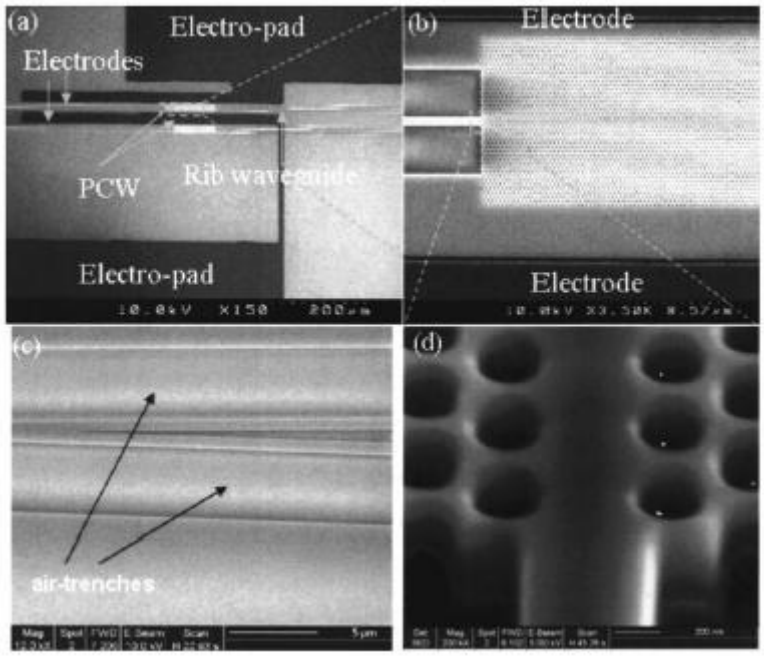

Figure. 3 SEM micrographs of the silicon PhC modulator: (a) the modulator. (b) detailed view of the PhC waveguide with two electrodes. (c) Y-junction. (d) Magnified PhC waveguide based on a triangular lattice with lattice constant a=400nm, hole diameter d = 210 nm, and top Si thickness t = 215 nm, buried oxide (BOX) SiO_2 thickness of 2 μm (from Ref. [24])

Note that the N-type Si substrate with 1×10^{14} cm^{-3} doping concentration is defined as intrinsic.[24] The fabrication process generally goes through the following steps. The PhC and Si rib waveguide structures are patterned with E-beam resist ZEP-520A by E-beam lithography (Jeol JBX6000). After developing the resist, the patterns are transferred to a 57 nm oxide mask layer by reactive ion etching (RIE) using CHF_3. Then the E-beam resist residue is removed by plasma ashing in oxygen. Using the oxide layer as a hard mask the patterns are transferred to the silicon core layer by a HBr and Cl_2 RIE process. Post-etching oxidation at 850^{o}C is implemented for about 1 minute. The post-etching oxidation forms an additional 5~7nm oxide layer, resulting in the sidewalls of the air-holes being significantly smoother than the original surface after dry etching. Extensive experimentation with various processes is conducted to determine the optimized process parameters. A proper pre-offset of the hole size in e-beam pattern design is used so that the hole size can be controlled with an accuracy of 5%. After the silicon photonic crystal waveguides and rib waveguides are fabricated, the regions for the aluminum electrodes and pads are patterned by a conventional photolithography mask aligner, followed by metal deposition and metal liftoff. Aluminum electrodes and pads are then sintered to form ohmic contacts with the top silicon layer. The SEM micrographs of the final structure are shown in Fig. 3.

2.4 Characterization

We characterized the optical transmission and dispersion of photonic crystal waveguide modes. It is crucial to develop a reliable method of measuring the optical transmission of photonic crystal waveguides. A simplistic approach for transmission measurement places a PCW between two straight Si rib waveguides. However, the stray light—light reaching the output through the air above the chip surface—in the forward direction is often strong enough to smear the signal transmitted via the rib-PCW-rib guided channel. To overcome this problem, we employed a waveguide bend,[24] which shifted the output fiber by at least 600μm and significantly suppressed the stray light collected by the output

fiber. The measurement illustrated in Fig. 4 was performed on a fully-automated Newport Photonics Alignment/Packaging Station. Two lensed fibers were manipulated by two automated 5-axis stages, which were controlled by a computer to precisely align the fibers with the rib waveguides. The input lensed fiber was aligned for the transverse electrical (TE) mode with the electric field vector primarily in plane. The TE polarized light was used for all the measurement presented here.

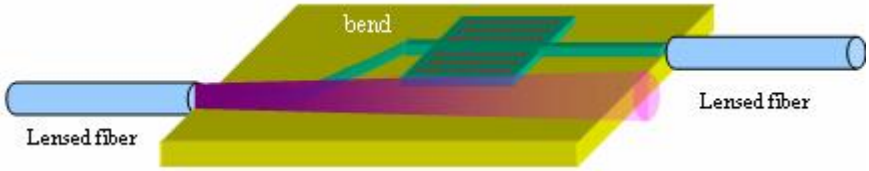

Figure 4 Test setup. Two lensed fibers are used for better mode matching. A waveguide bend is used to shunt the relatively intense stray light in the forward direction. This guideline applies to the measurement of both single waveguide and Mach-Zehnder modulator.

Micrographs of the Mach-Zehnder modulator are shown in Fig. 3. One branching point of the Mach-Zehnder modulator is shown in Fig. 3(c). In the active arm of the Mach-Zehnder structure, a photonic crystal waveguide of 80 μm in length is located between two 500 μm long electrodes, as shown in Fig. 3(a). The two ends of the photonic crystal waveguide are connected to two silicon rib waveguides. The rib waveguides are separated from two electrodes by two 4μm wide air trenches that are etched through the entire top silicon layer. Therefore, the rib waveguides are thermally and electrically isolated from the long electrodes (note the thermal conductivity of silicon oxide is much smaller than that of silicon). An 8μm wide metal wire passes over the lower silicon rib waveguide to connect one pad with the lower electrode. The details of this overpass metal wire will be discussed elsewhere. We note that a trivial overpass structure tends to fail because the metal wire is susceptible to structural disruption as it passes over the surface steps created by the silicon rib waveguide underneath.

We investigate the modulation performance of the fabricated modulators. We characterize the modulation depth and the minimum current needed for a π phase-shift of our silicon MZI modulator operating at 1567 nm. We have measured the transmission spectra which confirm that 1567 nm falls into the bandedge of the transmission spectra. The optical output intensity against drive current is shown in Fig. 5. The modulation depth of 92% is clearly seen in Fig. 5. The drive current to achieve π phase shift, I_π, is a typical measure of the modulation efficiency of such MZI modulator devices. The I_π of our silicon MZI modulator is as low as 0.15 mA compared to several milliamperes in conventional MZI modulator devices,[17-18] which shows the high modulation efficiency of our MZI modulator device. With a 50 Ω impendence matched lumped electrode structure, it would be equivalent to a V_π of 7.5 mV. The length of the modulator is reduced to 80 μm compared to several millimeters for the modulators using silicon rib waveguides in MZI structures, [15-16] due to the extraordinary dispersion of the PhC waveguide.

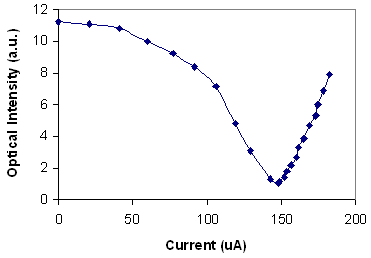

Figure 5 The plot of optical intensity vs. injection current for the silicon Mach-Zehnder modulator based on photonic crystal waveguides. (from Ref. [24])

Note that the injected current per unit waveguide length remains the same as in conventional waveguides. All of these prove the proposed advantages of using PhC waveguide instead of conventional rib waveguide mentioned above. The

thermo-optic effect is excluded as a mechanism for phase shift, because the power dissipation I^2R is very low, and the subsequent temperature modulation amplitude of the waveguide is less than 0.3°C according to preliminary simulations of heat transfer processes in the device.

In summary, silicon Mach-Zehnder modulators based on photonic crystal waveguides have been fabricated and tested. Modulation phenomena are observed with an ultra-short interaction length of 80μm and a peak drive current of 0.15mA. These characteristics are at least one order of magnitude better than conventional silicon waveguide modulators.

3. POLYMER PHOTONIC CRYSTALS FOR NANOPHOTONIC APPLICATIONS

3.1 Polymer nanophotonics and nano-imprint technique

Polymeric materials have exclusive advantages in transferability to different substrates. The polymeric nanostructures to be presented can be integrated with Si, GaAs, SiO_2, PC board and ceramics, which are attractive platforms for realizing dielectric waveguides and optoelectronic devices for emerging high market-value applications.[25] Photonic crystals provide new avenues of engineering polymeric nanostructures for optical applications. Particularly, polymeric photonic crystals can be manufactured by the nano-imprint technique.[26-27] The nano-imprint technique is especially suitable for high resolution applications and for three-dimensional replication of nanostructures.

3.2 Fabrication technique

Initially we were able to successfully fabricate a single waveguide of 600nm wide on a polymer by the nano-imprint technique. However, as we proceeded to fabricate an array of nanostructures, problems emerged. Particularly, when we imprinted a two-dimensional array of air holes to form a 2D photonic crystal, it was difficult to ensure the quality of all holes over a large area to meet an acceptable standard.

Later, we systematically investigated the sources of quality deviation from hole to hole over a large area. It was determined that the quality of the air holes was plagued by two issues: (1) The presence of air bubbles in the polydimethylsiloxane (PDMS) template and UV-curable polymer; (2) Localized damage and deformation of a PDMS template during the peeling-off processes.

One type of deformation called pairing is illustrated in Fig. 6. The pairing deformation was particularly severe for a 1D array of closely spaced narrow lines, or a 2D array of rods on a PDMS template.

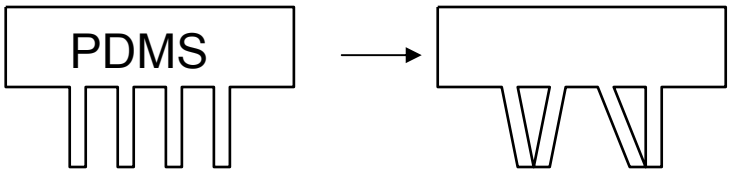

Figure 6 Deformation of a PDMS template: pairing of adjacent features in arrayed nanostructures.

Note that the localized deformation occurs in the course of both fabricating the PDMS template, and imprinting the UV-curable polymer, whereas the localized damage that causes PDMS to suffer irreparable attrition in shape primarily occurs during fabricating the PDMS template against a hard master (silicon).

To resolve these issues, we ran a number of trial processes with varying processing conditions. The quality of masters, PDMS templates, and photonic crystals made on UV-curable polymer was monitored after each step with optical and electronic microscopy. The following countermeasures were determined

- Use soft material for the master to minimize the attrition of the PDMS
- Using "positive" structures on the master
- Optimize the pressure, temperature, and timing of the baking and curing processes for PDMS, and the UV-curable polymer.

We evaluated a number of alternative materials, including silicon, silica glass, and e-beam resists, for the master. Thus far, we have derived satisfactory results using e-beam resists because the resists are soft materials which reduce the possibility of causing irreparable attrition to the PDMS template. In addition, using e-beam resists as the master directly saves the extra dry etching process to transfer the patterns to the underlying hard materials compared to using silicon or silica glass as the master. Note that in Fig. 7(a), a specific e-beam resist ZEP-520A is depicted as the material for the master.

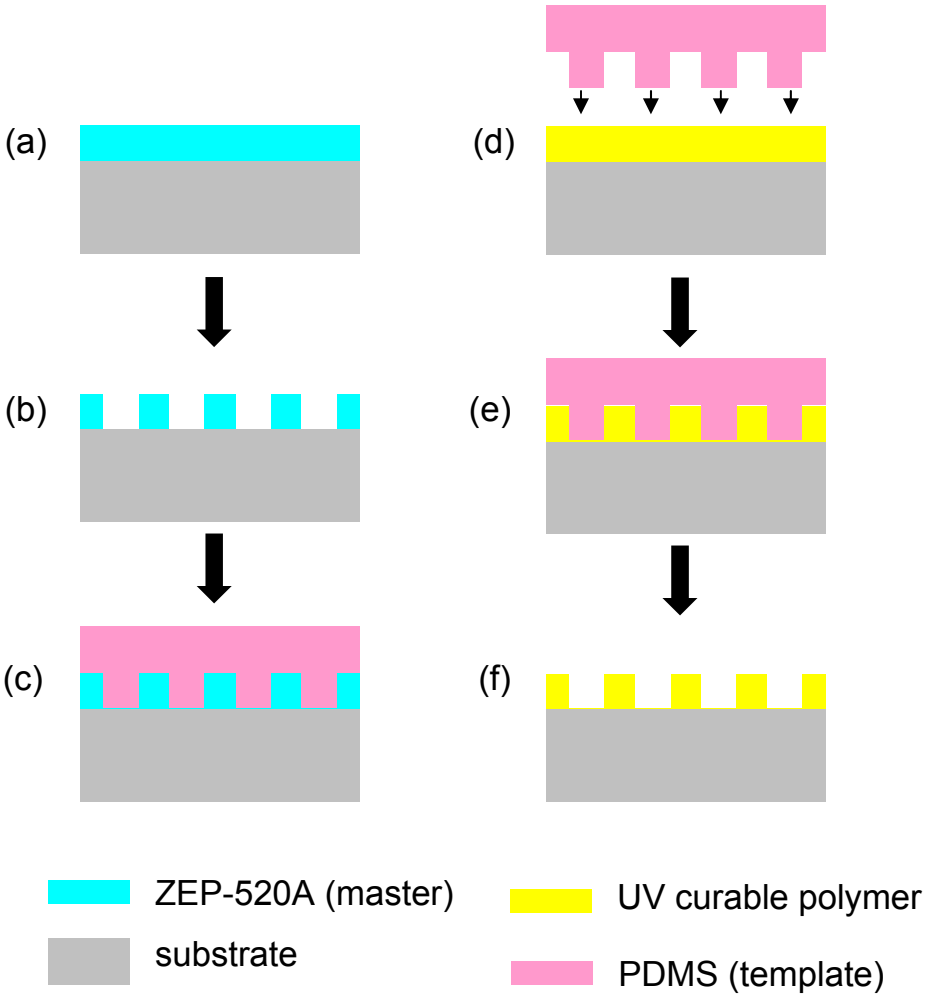

Figure 7 Outline of fabrication process flow (a) coat ZEP520A, (b) pattern by e-beam nanolithography to form master, (c) form PDMS template, (d) coat UV curable polymer, (e) apply template ("stamping") and curing, (f) remove template.

In the second countermeasure, "positive" refers to the type of resist used. For a positive e-beam resist, the exposed areas are removed. Generally, for photonic crystal structures, this corresponds to the air hole structure. For a negative e-beam resist, the exposed areas remain after developing the resist; this gives an array of rods in the air. If we simply intend to make a perfect PDMS template, then the negative e-beam resist is preferred. This is because in the fluidic state prior to curing, the PDMS can easily flow around the rods to fill every recess of the surface topology and faithfully reproduce the desired pattern—an array of air holes. However, we still have a subsequent process where we will be using the "positively" patterned PDMS template to imprint on the UV-curable polymer. Then the trouble arises because the solution that contains the polymer will have difficulties filling in small holes in the PDMS template; this gives rise to the wide presence of air bubbles. Now it is very clear: with a negative e-beam resist, the PDMS template can be easily

fabricated, but imprinting the polymer tends to suffer from the presence of air bubbles; with a positive e-beam resist, the fabrication of PDMS template tends to encounter the problem of air bubbles, whereas the imprinting process will proceed smoothly. We selected the positive e-beam resist based on the following observation. During the process of fabricating the PDMS template [Fig. 7(c)], the top surface of the PDMS is open to the ambient. If air bubbles are present in the PDMS, it is relatively easy to drive them out during the template fabrication. In the course of imprint the UV-curable polymer [Fig. 7(e)], the top surface of the polymer solution is covered by the PDMS template. It is extremely hard to drive the air bubbles out of the UV curable polymer solution—the best approach is to suppress the air bubbles from being formed. In summary, using a positive resist, air bubbles are present in the PDMS template fabrication, but can be driven out; using a negative resist, air bubbles tend to be rampant in the imprinting process and are hard to remove. Another important consideration is related to the manufacturing potential. Fabricating the template only comprises a small part of time and effort of the whole fabrication process whereas the imprinting the polymer will use the template repeatedly. Therefore, we can afford more time and effort to make a perfect template, but it is desired that the imprinting process is as easy as possible. Using the positive e-beam resist, we exactly resonate with this manufacturing related consideration.

Lastly, optimizing the pressure, temperature, and timing of the baking and curing processes involved an extended effort of trial-and-error, and our experience in imprinting much larger features also supplied empirical guidance.[28] The complete process is delineated below:

1. Coat e-beam resist ZEP-520A on a substrate, Fig. 7(a)
2. Pattern ZEP-520A using e-beam nanolithography followed by developing the exposed areas. The sample is placed on a hotplate at 40^{o}C for 10 minutes. Fig. 7(b)
3. Prepare PDMS mixture. The mixture is placed in a vacuum oven with the pressure set to slightly below 1atm. To preclude sudden burst of air bubbles, a slow process at room temperature is executed for 30~60minutes.to complete remove air bubbles.
4. Apply PDMS mixture on the patterned ZEP-520A. The sample is placed in a vacuum oven for 30 minutes with the pressure set to slightly below 1atm and the temperature set to 40^{o}C.
5. The sample is placed on a hotplate for 24 hours with the temperature set to 40^{o}C, then the cured PDMS template is taken off from the surface.
6. Coat UV-curable polymer on a substrate;
7. Apply PDMS template on the top, Fig. 7(d). To minimize the presence of air bubbles, the sample is placed in a vacuum oven for 2 hours at room temperature with the pressure set to slightly below 1atm;
8. Cure the polymer by ultra-violet irradiation through the PDMS template, Fig. 7(e)
9. Peel-off the PDMS template, Fig. 7(f). Post-bake at 160^{o}C, N_2 atmosphere, 2 minutes

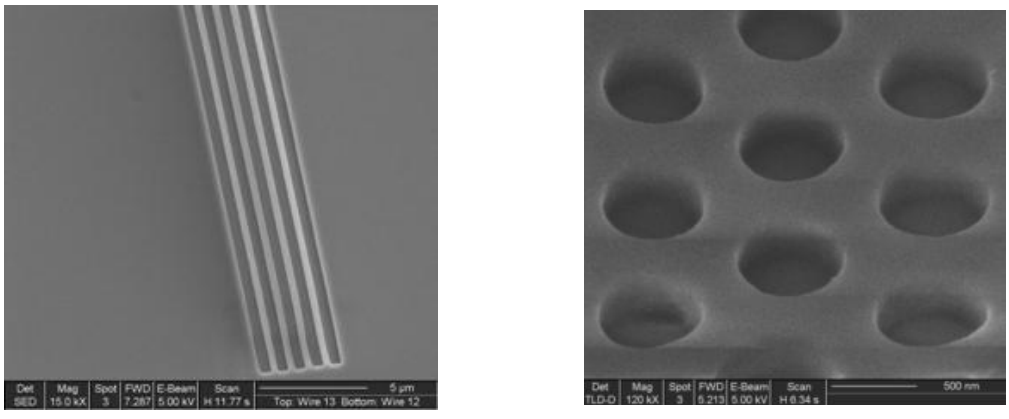

(a) (b)

Figure 8 Imprinted polymeric nanostructures (a) 200nm lines (b) Photonic crystal structures with highly smooth surface and side wall.

3.3 Characterization

With the above processes, we have been able to significantly improve the quality of photonic crystals and waveguide arrays. The polymer structures fabricated by the nano-imprint technique were examined by scanning electron microscopy (SEM). The SEM micrographs shown in Fig. 3 illustrate the high quality of the structures we have produced through our efforts. In an early stage, we were able to fabricate a single polymer waveguide of 600nm wide. In a later stage, we have fabricated arrays of waveguides as narrow as 100nm with high uniformity. As shown in Fig. 8(b), both the uniformity and quality of the air holes are satisfactory. No defects are present in the polymer photonic crystal.

Note in the preceding discussions, it was implied that patterns being fabricated will be reversed for the positive and negative e-beam resists respectively. In principle, any pattern can be fabricated by either a positive resist or a negative resist. However, the preceding restriction associated with positive and negative resists is due to the connectivity of the removed resist region, which is related to the ease of removing the air bubble in the structures. We believe that with intensive efforts, this fabrication restriction on the connectivity can be lifted. However, we do not feel this issue will be critical for the 3D photonic crystals we plan to make. Whatever the connectivity of the removed resist region, a 3D photonic crystal can always be constructed to exhibit the superprism effect and beam scanning capability with proper design. Furthermore, although PDMS has been used to fabricate the currently reported samples, the experience we accrued can be transferred easily to other template materials as well. Further efforts of fabricating 3D photonic crystal structures are underway and will be reported elsewhere.

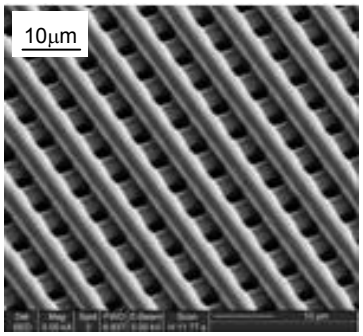

Figure 9 3D woodpile photonic crystal fabricated on SU-8

4. SUMMARY

An ultra-compact silicon modulator was experimentally demonstrated based on silicon photonic crystal (PhC) waveguides. Modulation operation was achieved by carrier injection into an 80 μm-long silicon PhC waveguide of a Mach-Zehnder interferometer (MZI) structure. The driving current to obtain a phase shift of π, I_π, across the active region was as low as 0.15 mA. The modulation depth was 92%. The electrode between the two waveguide arms of the MZI structure was the routed to the space outside the MZI. In real devices, this planarized routing design would be essential to integrating the silicon modulator with electrical driving circuitry on a single silicon chip. For laboratory test, this routing design also eliminated the need of placing a bulky pad between the two arms and gave our modulator a smaller footprint. Polymeric photonic crystals were designed, and were fabricated by the nano-imprint technique.

5. ACKNOWLEDGMENTS

This work is supported in part by AFOSR and AFRL. Technical advice from Drs. Gernot Pomrenke, Richard Soref, and Rob Nelson is acknowledged. The authors acknowledge partial support from the State of Texas and SEMATECH under the AMRC program. The devices were fabricated at UT MRC with nanofabrication facilities partially supported under NSF's NNIN program. We thank the CNM of UT Austin, Welch Foundation and SPRING for partial support of the Dual Beam FIB/SEM usage.

REFERENCES

1. E. Yablonovitch, "Inhibited Spontaneous Emission in Solid-State Physics and Electronics," *Phys. Rev. Lett*., **58**,2059 (1987).
2. S. John, "Strong localization of photons in certain disordered dielectric superlattices," *Phys. Rev. Lett*., **58**, 2486 (1987).
3. M. Notomi, K. Yamada, A. Shinya, J. Takahashi, C. Takahashi, and I. Yokohama, "Extremely Large Group-Velocity Dispersion of Line-defect Waveguides in Photonic Crystal Slabs," *Phys. Rev. Lett.*, **87**, 253902 (2001).
4. S. J. McNab, N. Moll, and Y. A. Vlasov, "Ultra-low loss photonic integrated circuit with membrane-type photonic crystal waveguides", *Optics Express*, **11**, 2927, (2003).
5. D. W. Prather et. al., "Dispersion-based optical routing in photonic crystals", *Optics Letters*, **29**, 50 (2004).
6. T. J. Karle, Y. J. Chai, C. N. Morgan, I. H. White, T. F. Krauss, Observation of Pulse Compression in Photonic Crystal Coupled Cavity Waveguides *J. Lightwave Technology*, **22**, pp. 514 – 519 (2004).
7. M Soljacic, S. G. Johnson, S. Fan, M. Ibanescu, E. Ippen, J. D. Joannopoulos, "Photonic-crystal slow-light enhancement of nonlinear phase sensitivity ," *J. Opt. Soc. Am.* B **19**, 2052 (2002).
8. M. Soljacic, J.D. Joannopoulos, "Enhancement of nonlinear effects using photonic crystals," *Nature Materials*, **3**, 211 (2004).
9. R. A. Soref, B. R. Bennett, "Electrooptical Effects in Silicon," *IEEE J. Quantum Electron.* **QE-23**, 123 (1987).
10. R. A. Soref, "Silicon photonics technology: past, present, and future," *Proc. SPIE*, **5730**, 19 (2005).
11. G. Reed, A. P. Knights, *Silicon Photonics, An Introduction*, John Wiley & Sons, Hoboken, NJ (2004).
12. R. T. Chen, L. Lin, C. Choi, Y. J. Liu, B. Bihari, L. Wu, S. Tang, R. Wickman, B. Picor, M. K. Hibbs-Brenner, J. Bristow, and Y. S. Liu, "Fully embedded board level optical interconnects," *Proc. IEEE* **88**, 780 (2000).
13. Pavesi, L., Negro, L. D., Mazzoleni, C., Franzo, G. & Priolo, F. "Optical gain in silicon nanocrystals," *Nature*, **408**, 440–444 (2000).
14. Haisheng Rong, Richard Jones, Ansheng Liu, Oded Cohen, Dani Hak, Alexander Fang & Mario Paniccia, "An All-silicon Raman laser," *Nature* **433**, 292-294 (2005).
15. A. Liu, R. Jones, L. Liao, D. Samara-Rubio, D. Rubin, O. Cohen, R. Nicolaescu, and M. Paniccia., "A high-speed silicon optical modulator based on a metal-oxide-semiconductor capacitor," *Nature* **427**, 615 (2004).
16. G. Cocorullo, M. Iodice, I. Rendina, and P. M. Sarro, "Silicon thermaloptical micromodulator with 700-kHz-3-dB bandwidth*," IEEE. Photon. Technol. Lett.*, **7**, 363 (1995).
17. G. V. Treyz, "Silicon Mach-Zehnder waveguide interferometer operating at 1.3 μm", *Electronics Letters*, **27**, 118 (1991).
18. U. Fischer, T. Zinker, B. Schuppert and K. Petermann, "Singlemode optical switches based on SOI waveguides with large cross-section," *Electronics Letters*, **30**, 406 (1994).
19. Tao Chu, Hirohito Yamada, Satomi Ishida, and Yasuhiko Arakawa, "Thermooptic switch based on photonic-crystal line-defect waveguides," *IEEE. Photon. Technol. Lett*, **17**, 2083 (2005).
20. R. L. Espinola, M. –C. Tsai, James T. Yardley, and R. M. Osgood, "Fast and low-power thermooptic switch based on thin silicon-on-insulator," *IEEE. Photon.Ttechnology Lett.*, **15**, 1366 (2003).
21. P. Sewell, K Biwojino, S. Sujecki, and T. M. Benson, "A thermal model for silicon-on-insulator-based waveguide modulators," *ICTON*, 151 (2002).
22. C. Z. Zhao, G.Z. Li, E.K. Liu, Y. Gao, and X.D. Liu, "Silicon on insulator Mach-zehnder waveguide interferometers," *Appl. Phys. Lett.* **67**, 2448 (1995).
23. G. V. Treyz, P.G. May and J.M. Halbout, "Silicon Mach-Zehnder waveguide interferometers based on the plasma dispersion effect" *Appl. Phys. Lett*., **59**, 771 (1991).
24. Y. Jiang, W. Jiang, L. Gu, X. Chen, R. T. Chen, "80-micron interaction length silicon photonic crystal waveguide modulator," *Appl. Phys. Lett.* **87**, 221105 (2005).
25. Ray T. Chen, "Polymer-based Photonic Integrated Circuits," (Invited Review), *Optics and Laser Technology*, **25**, pp. 347-365 (1993).
26. M. Colburn, A. Grot, M. Amistoso, B. J. Choi, T. Bailey, J. Ekerdt, S. V. Sreenivasan, J. Hollenhorst, C. G. Willson, "Step and Flash Imprint Lithography for sub-100nm Patterning" *Proc. SPIE*, **3999**, 453-457 (2000).
27. M. Colburn, T. Bailey, B.J. Choi, J.G. Ekerdt, S.V. Sreenivasan, C.G. Willson; "Development and Advantages of Step-and-Flash Lithography"; *Solid State Technology*; **46**(7) 67 (2001).

28. L. Wang, X. Wang, W. Jiang, J. Choi, R. T. Chen, "45° Polymer-based Total Internal Reflection Coupling Mirrors for Fully-Embedded Intraboard Guided Wave Optical Interconnects," *Appl. Phys. Lett.*, **87**, 141110 (2005).